

# Kirigami Strain Sensors Microfabricated From Thin-Film Parylene C

Alex Baldwin<sup>✉</sup> and Ellis Meng<sup>✉</sup>, *Fellow, IEEE*

**Abstract**—A kirigami-based strategy was investigated for strain transduction, using serpentine gold traces embedded in thin-film Parylene C. Multiple kirigami slit designs were evaluated via COMSOL simulation and mechanical force testing; sensors having tightly packed slits stretched up to 17.5 mm (350% strain) before mechanical failure and 9 mm (180% strain) before electrical failure. Strain transduction was achieved by monitoring DC resistance changes during stretching. DC resistance linearly increased with strain, with sensitivities up to 0.16  $\Omega/\text{mm}$  (gauge factor = 0.007) and minimal hysteresis. High-frequency trace impedance and inter-trace capacitance were also investigated during strain cycling. Capacitance increased with strain and high-frequency impedance show a nonlinear strain relationship. The biocompatible construction and extremely low profiles (20  $\mu\text{m}$  thick) of these sensors are attractive for minimally invasive *in vivo* strain sensing applications. [2018-0130]

**Index Terms**—Electromechanical sensors, kirigami, microsen-sors, microfabrication, Parylene C, strain sensors, thin film sensors.

## I. INTRODUCTION

KIRIGAMI is a paper cutting technique often used to complement origami. By strategically placing cuts in a planar substrate and then subjecting the substrate to tension or compression, complex three-dimensional patterns can be produced [1]–[3]. Research groups in several fields implemented kirigami techniques for manufacturing, packaging, actuation, or sensing [4]–[7]. When applied to thin film devices such as microelectromechanical systems (MEMS), kirigami enables complex three-dimensional structures using only two-dimensional planar microfabrication techniques [8]. Several groups reported lithium-ion batteries or supercapacitors fabricated using kirigami patterns [7], [9], [10]. These devices were first fabricated on a planar substrate, then released and folded into their final, packaged shape. Kirigami devices can also generate out-of-plane movement from linear displacement or applied force; applications include sun-tracking solar

cells [11], dynamic mechanical filters with tunable properties [12], and tunable diffraction gratings [13]. Combined with piezoelectric or pneumatic actuation, kirigami can be used to produce complex motion from simple one-dimensional forces. Mechanical hands [14], biomimetic robots [15], [16], piezoelectric energy harvesters [17], and artificial muscles [18] that combine kirigami techniques with actuators were reported.

A common kirigami technique is the use of offset rows of slits to enable a material to stretch far beyond what its normal tensile properties would allow. By converting tensile stress to torsion, a kirigami slit pattern allows linear movement over a high dynamic range without compromising the substrate's structural integrity [13], [19]. Kirigami slits were utilized in graphene to achieve up to 267% strain before mechanical failure [20]–[22], while on Parylene C substrates, strain up to 1100% was reported [23], [24]. Slotted kirigami devices exhibit minimal stress between slits, suggesting that conduction paths placed in these regions will exhibit electronic stability. By introducing non-uniform conduction paths and selectively increasing trace resistance in regions which tend toward either compressive or tensile strain, a trace's DC electrical resistance can correlate with strain [25]. Flexible strain sensors typically exhibit relatively low strain operation [25], [26]. The potential combination of flexible, thin-film Parylene C with kirigami slit patterns could enable strain sensors with much higher dynamic ranges.

## II. SENSOR DESIGN

To test kirigami patterns for stretchable Parylene C electronics, devices with serpentine traces wound among an etched kirigami slit array were designed and fabricated (Fig. 1). Each film contained eight gold traces sandwiched between 10  $\mu\text{m}$  thick Parylene C layers with each trace forming a single device. Parylene C is highly flexible but has low elongation at break (between 20 and 25% [27], [28]). However, Parylene C's compatibility with oxygen plasma etching allows fabrication of precisely aligned, high aspect ratio kirigami slits [29], [30] which permit operation exceeding the limits of the contiguous film.

Each device consisted of a kirigami slit array 5 mm long by 4 mm wide with contact pads at either end. Slit dimensions were held constant at 600  $\mu\text{m}$  long and 20  $\mu\text{m}$  wide. Slit ends were capped with 50  $\mu\text{m}$  diameter circles to avoid stress concentration. However, lateral etching of Parylene during deep reactive ion etching caused feature wash-out and resulted in rounded slits 600  $\mu\text{m}$  long and 50  $\mu\text{m}$  wide. Two variations of the kirigami slit array were designed: A-type devices contained slits spaced 400  $\mu\text{m}$  apart with inter-row spacing

Manuscript received June 10, 2018; revised August 8, 2018; accepted September 3, 2018. Date of publication September 19, 2018; date of current version November 29, 2018. This work was supported in part by the U.S. National Science Foundation under Grant EFRI-1332394, in part by the USC Provost's Fellowship, and in part by the Alfred E. Mann Institute Fellowship. Subject Editor H. Jiang. (Corresponding author: Ellis Meng.)

A. Baldwin is with the Department of Biomedical Engineering, University of Southern California, Los Angeles, CA 90089 USA (e-mail: axbaldwin@gmail.com).

E. Meng is with the Department of Biomedical Engineering, University of Southern California, Los Angeles, CA 90089 USA, and also with the Ming Hsieh Department of Electrical Engineering, University of Southern California, Los Angeles, CA 90089 USA (e-mail: ellis.meng@usc.edu).

This paper has supplementary downloadable material available at <http://ieeexplore.ieee.org> provided by the authors.

Color versions of one or more of the figures in this paper are available online at <http://ieeexplore.ieee.org>.

Digital Object Identifier 10.1109/JMEMS.2018.2869090

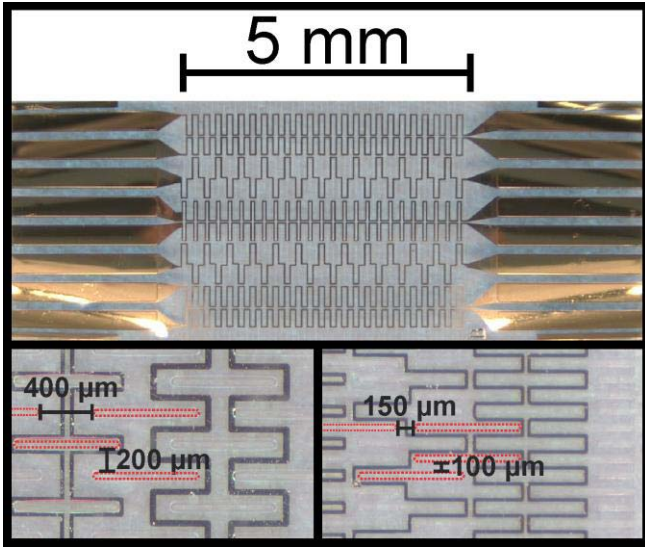


Fig. 1. Top: Parylene C kirigami strain sensors consist of a 5 mm by 4 mm region containing gold traces within a kirigami slit array, with contact pads at either end. Bottom left: A-type devices contained slits spaced 400  $\mu\text{m}$  apart in offset rows, with 200  $\mu\text{m}$  separation between rows. Bottom right: B-type devices contained slits spaced 150  $\mu\text{m}$  apart in offset rows with 100  $\mu\text{m}$  separation.

of 200  $\mu\text{m}$ , while slits in B-type devices were spaced 150  $\mu\text{m}$  apart in offset rows every 100  $\mu\text{m}$ . Serpentine gold traces between 10 and 20  $\mu\text{m}$  wide with nominal DC resistance values between 50 and 150  $\Omega$  were wound throughout the slit array.

The design of the kirigami devices was selected to achieve high strain operation based on the guidelines that the length  $L$  of each slit is greater than the distance  $d$  between slits, both in the vertical and lateral directions ( $L > d$ ) [19]; the  $L : d$  ratio of B-type devices was 4:1, indicating that devices will be capable of high-strain operation, while A-type devices had an  $L : d$  ratio of 3:2, indicating that elastic operation will only occur over a limited strain range. In addition, slit width and minimum trace width were constrained based on lithography resolution for etch and liftoff resists, and the spacing between slits in B-type devices was selected as the minimum spacing necessary for two 20  $\mu\text{m}$  wide traces to pass between slits while reserving enough space for fabrication variability and overetching. A-type devices were designed with twice the vertical separation between slits as B-type devices. Slit length (600  $\mu\text{m}$ ) was chosen such that eight strain sensors (each sensor consisting of a single gold trace with contact pads at each end) could be placed on each fabricated die. Additional devices with slits 1200  $\mu\text{m}$  long and slit spacing identical to B-type devices were also designed and fabricated but were too delicate for successful testing.

### III. SIMULATION

Stress concentration and elongation to break in both A- and B-type kirigami devices were investigated using a simple finite element model. Simulations were performed using COMSOL Multiphysics 4.3 (COMSOL Inc., Stockholm, Sweden). Mechanical models were constructed for the active

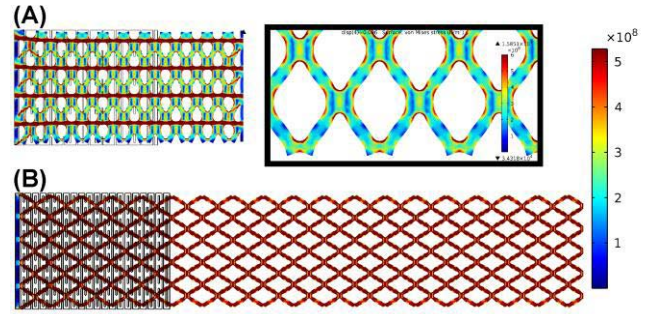


Fig. 2. The von Mises stress in Pascals within (A) A-type and (B) B-type kirigami devices. B-type devices exhibited much lower stress under comparable strain than A-type devices. Strain is shown at a 1:1 scale, with an outline showing the geometry of the unstretched device. Inset: stress in B-type devices is concentrated near the ends of each slit.

regions of both A- and B-type kirigami devices; models measured 5 mm long, 4 mm tall, and 20  $\mu\text{m}$  thick, with slit dimensions and spacings identical to the fabrication masks for the experimental devices. Material properties of Parylene C were based on literature from Specialty Coating Systems, Inc., which manufactures Parylene dimer and deposition systems [31]. The material was assumed to be isotropic. To determine elongation to break, the left end of the device was held in place while the right end was displaced at intervals of 0.1 mm. For each displacement, the von Mises stress was calculated throughout the device; when the maximum von Mises stress within a device exceeded Parylene C's reported yield strength of 3200 MPa [31], mechanical failure was said to occur.

The stress in A-type devices exceeded the yield strength of Parylene C after only 1.7 mm displacement (34% strain), while the stress in simulated B-type devices did not exceed Parylene C's yield strength until 11.8 mm displacement (236% strain). Simulated stress inside A-type devices concentrated in four lateral bands between offset rows of slits, while stress in B-type devices was more uniform, concentrating near the ends of each slit (Fig. 2).

### IV. FABRICATION AND TESTING METHODS

Both A- and B-type kirigami devices consisted of Parylene C layers sandwiching gold traces. Devices were fabricated using previously reported micromachining techniques [29], [30]. First, 10  $\mu\text{m}$  of Parylene C was deposited onto a 4" prime silicon wafer using an SCS LabCoter 2 deposition system (Specialty Coating Systems, Indianapolis, IN, USA). A 200  $\text{\AA}$  titanium adhesion layer and 2000  $\text{\AA}$  of gold were then deposited using a Temescal electron-beam metal deposition system and patterned via liftoff using a 2  $\mu\text{m}$  thick layer of AZ 5214 image reversal photoresist (Integrated Micro Materials, Argyle, TX, USA). A second 10  $\mu\text{m}$  layer of Parylene was deposited as insulation, then a 15  $\mu\text{m}$  thick etch mask of AZ P4620 photoresist (Integrated Micro Materials, Argyle, TX, USA) was spin coated and patterned via UV lithography. The slit array was etched in an Oxford PlasmaLab 100 inductively coupled plasma etcher (Oxford Instruments, Abingdon, UK) using a switched-chemistry deep reactive ion etch, with oxygen plasma as the etchant and  $\text{C}_4\text{F}_8$  for passivation. This etching process can generate high aspect ratios in Parylene C,

with sidewall angles exceeding  $70^\circ$  [32]. Contact pads and device cutouts were exposed with a second, lower power deep reactive ion etch using a  $15\ \mu\text{m}$  thick AZ4620 etch mask. To prevent gold sputtering, RF power during the second etch was lowered so that voltage did not exceed 70V. After fabrication, wafers were cleaned by immersion in acetone, isopropyl alcohol, and deionized water for 10 minutes each. Then devices were released from the silicon carrier wafer by gently peeling while immersed in deionized water. Overetching of slits and the device cutout were necessary since peeling devices off the carrier wafer could result in the destruction of the delicate kirigami slit array.

Electrical connection was achieved by attaching a PEEK (polyether-ether-ketone) backing to contact pads using cyanoacrylate glue and inserting both ends into zero insertion force (ZIF) connectors (8 channel, 0.5 mm pitch; Hirose Electric Co. Ltd., Tokyo, Japan) [33]. Stretch testing of devices was accomplished by immobilizing one end and displacing the other end at 0.2 mm/s using a ThorLabs Z812 motorized stage. For mechanical testing, force was measured using a calibrated force gauge. For electrical testing, DC resistance was measured using a Keithley 2400 SourceMeter, and high-frequency electrical testing was performed using an Agilent E4980A precision LCR meter. All data was collected using a custom LabVIEW program. Testing first involved stretching devices to failure while measuring the mechanical forces involved and the DC trace resistance. Then, strain transduction was evaluated by measuring the DC resistance of traces over multiple stretch cycles within the device's elastic strain regime. Finally, the high-frequency electrical properties of each trace were investigated during repeated strain cycling.

## V. RESULTS

### A. Mechanical Testing

Devices with A-type and B-type slit arrays were stretched until mechanical failure while measuring the applied force. Identical devices without etched kirigami slits were tested as a control. Three devices of each type were stretched until tearing occurred while measuring the resultant force generated by each device. Displacement was defined as the linear distance from the unstretched sensor along the axis between contact pad regions, and strain was defined relative to the length of the slit array (5 mm displacement = 100% strain). Both A- and B-type kirigami slits drastically increased the distance that devices could stretch before breaking (Fig. 3).

Kirigami devices have been shown to possess nonlinear stretching dynamics, with three key regions appearing on force-displacement curves [19], [34]. Region I corresponds to an initial in-plane deformation of the material between slits, and is characterized by a linear force-displacement relationship. Region II is characterized by a flat force-displacement relationship, due to the transition from in-plane deformation to out of plane deformation in the form of rotation between slits. In region III, plastic deformation begins at the tips of slits, resulting in a transition back to a linear force-displacement relationship and eventually to device tearing and failure. All three of these regions were visible in the force-

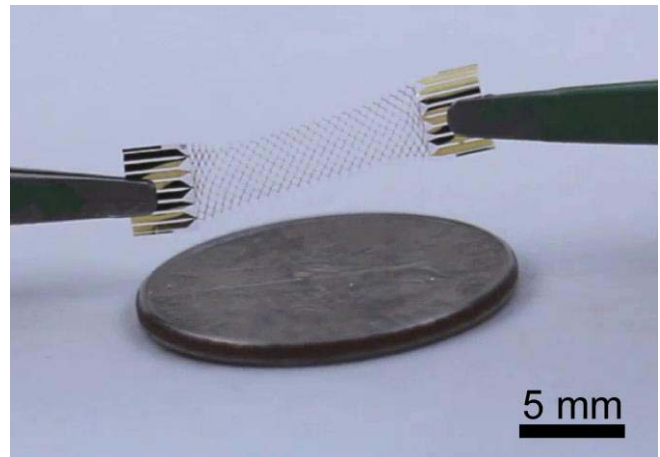


Fig. 3. A B-type kirigami devices shown stretched to about 10 mm displacement (200% strain), shown compared to an American 10 cent coin.

displacement curves generated for both A- and B-type kirigami devices (Fig. 4). The control device without etched kirigami slits experienced plastic deformation immediately and tore at 14% strain.

A-type devices appeared to plastically deform after only 4-6 mm displacement (80-120% strain), while B-type devices remained in the elastic regime until 10 to 12 mm displacement (200-240% strain). On average, A-type devices failed via tearing at 101% strain, corresponding to 0.7 N of force, while B-type devices failed at 350% strain and 0.3 N of force. Parylene devices without slits broke almost immediately (14% strain) with approximately 2 N of force.

### B. Electrical Testing

Electrical integrity of traces during stretching was evaluated by measuring the DC resistance of traces on an A-type and a B-type kirigami device while stretching to failure. DC resistance on A-type device traces was stable through 3.2 mm displacement (64% strain), then increased exponentially until open circuit failure occurred at 3.8 mm displacement (78% strain). B-type trace resistance stayed stable through 6 mm displacement (120% strain) and failed at 9 mm displacement (180% strain) (Fig. 5). Microcracks in the Parylene C were observed at inflection points near the ends of slits.

### C. Strain Transduction

Kirigami devices were evaluated for strain sensitivity, with the goal of developing a thin-film Parylene C strain sensor. Six gold traces across two B-type kirigami devices were tested; because of their greater mechanical and electrical stability, only B-type devices were evaluated for strain transduction. DC trace resistance was measured during repeated cycling from 0-4 mm displacement, revealing a positive linear correlation between resistance and strain (sensitivity 0.10-0.16  $\Omega/\text{mm}$ ) (Fig. 6). Gauge factor (GF), which is defined as the ratio of relative change in resistance to mechanical strain [35], varied between 0.004 and 0.007 for DC resistance-based strain transduction. Measurement noise



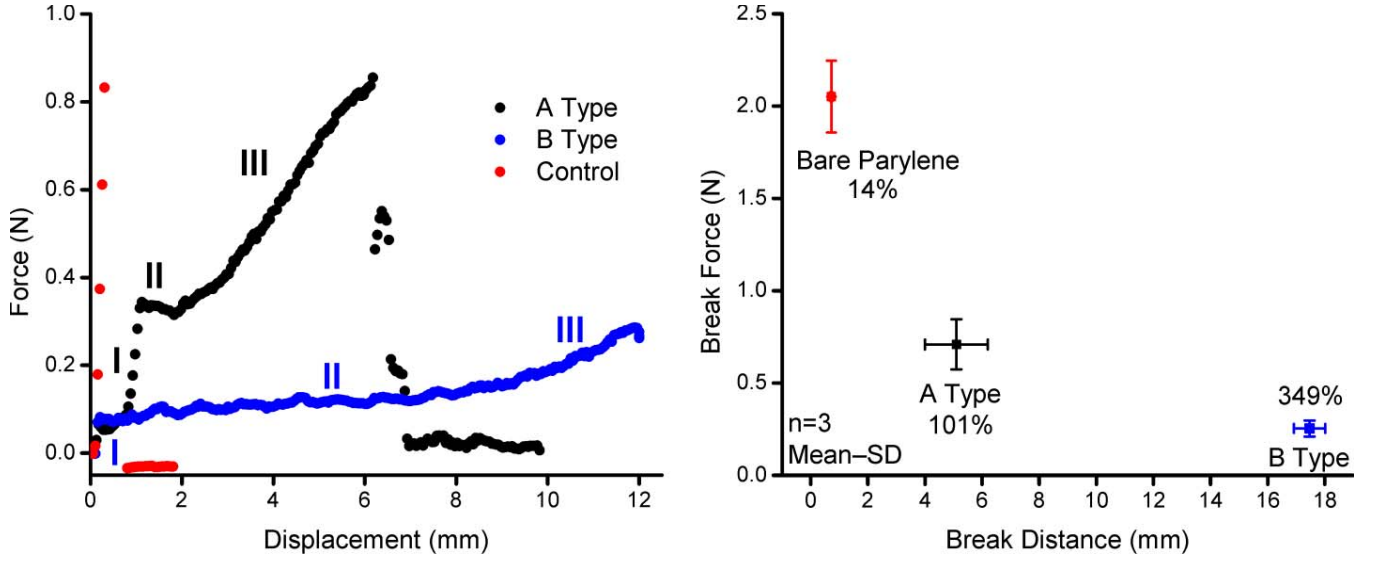


Fig. 4. Left: Representative force-displacement curves for A- and B-type devices, compared with identical Parylene devices without kirigami slits (control). When stretched, kirigami devices first experience brief in-plane displacement resulting in a linear force-displacement relationship (Region I), then a sharp transition to out of plane displacement and a flat force-displacement relationship (Region II), which lasts until plastic deformation begins and devices fail (Region III). Right: A-type devices failed at around 101% strain, while B-type devices failed at around 349% strain. Devices without slits failed almost immediately (14% strain). Break force was inversely proportional to break distance.

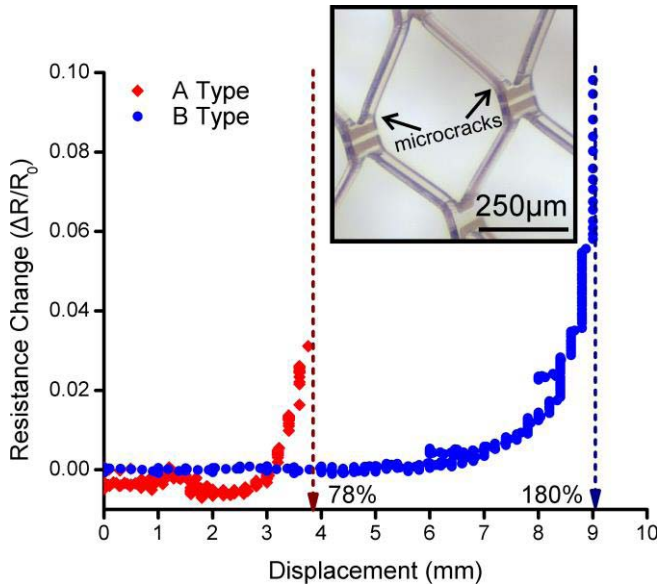


Fig. 5. The DC resistance of a trace on A- and B-type devices stretched until failure. Tighter slit spacing increased distance to failure from 78% to 180% strain. A-type traces have a lower DC resistance than B-type traces due to shorter path length; the baseline resistance of A-type traces is approximately 50  $\Omega$  versus 110  $\Omega$  for B-type traces. Any relationship between strain and resistance within the elastic deformation range is not visible in this figure due to its small magnitude compared to the large resistance changes seen during failure. Inset: Microscope image of a B-type device stretched to 9 mm (180% strain). Microcracks are visible near slit inflection points.

was significant compared to the sensor's sensitivity, resulting in  $3\sigma$  resolution between 0.2 and 1.6 mm (4 to 32% strain). A small amount of hysteresis was observed over multiple stretch cycles. Though noisy, the sensitivity of resistance to strain was observed to be stable over multiple strain cycles; there was no difference in sensitivity between the first time a device was stretched and subsequent stretching (Fig. 7).

#### D. High-Frequency Impedance Characterization

The high-frequency impedance magnitude of a single trace and the capacitance between adjacent traces were tested on two B-type kirigami devices. The goal of this preliminary impedance characterization was to identify future development paths for wireless strain transduction; devices were not optimized for impedance-based strain sensing, and the effects of strain on trace self-impedance or inter-trace capacitance was not considered when designing the devices. Four traces (sensors) on a single B-type kirigami device were tested for self-impedance, and a second kirigami device was evaluated for capacitance between traces.

Complex impedance at 2 MHz was recorded for single traces during multiple displacement cycles from 0-5 mm. The complex impedance of a trace includes the trace resistance  $R$ , self-inductance  $L$ , and self-capacitance  $C_s$ , and has the relationship

$$Z = \frac{R}{1 + j\omega RC_s} + j\omega L \quad (1)$$

where  $\omega$  is measurement frequency and  $j$  is  $\sqrt{-1}$ . Impedance magnitude showed a nonlinear dependence on strain, which varied depending on trace geometry (Fig. 8). The total increase in impedance magnitude between 0 and 5 mm displacement varied between 0.4% and 1%. The capacitance between adjacent traces ( $C_p$ ) at 100 kHz was also evaluated. Capacitance was relatively stable up to 2 mm displacement and increased linearly at a rate of 4.7 fF/mm between 2 and 5 mm displacement (Fig. 9).

#### VI. DISCUSSION

Experimental results showed that kirigami devices fabricated out of Parylene C and gold stretched to  $4.5\times$  their original size before mechanical failure (see supplemental video). The strain until mechanical failure in experimental

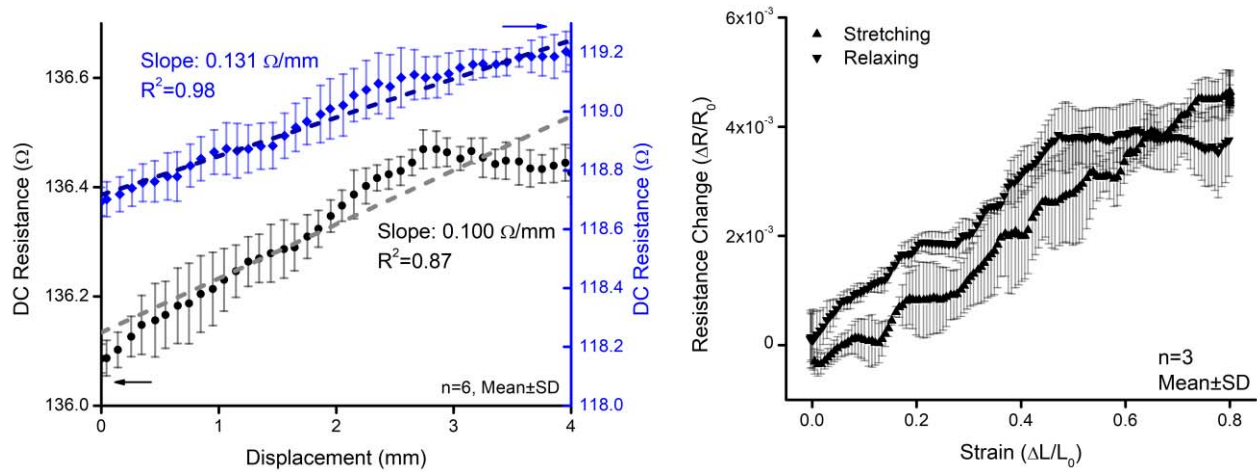


Fig. 6. Left: The DC resistance of two different traces on a single B-type kirigami device during strain cycling. The top trace showed a strain sensitivity of  $0.131 \Omega/\text{mm}$  ( $GF = 0.005$ ) with  $3\sigma$  resolution of  $1.07 \text{ mm}$  (21.4% strain), while the bottom traces had a strain sensitivity  $0.100 \Omega/\text{mm}$  ( $GF = 0.004$ ) with  $3\sigma$  resolution of  $0.81 \text{ mm}$  (16.2% strain). Mean and standard deviation were calculated using resistance values measured at  $0.1 \text{ mm}$  intervals while increasing and decreasing strain over three strain cycles. Both traces are the same design; differences in baseline resistance were likely due to process variations. Right: DC resistance change versus strain for a different gold trace over three displacement cycles between  $0$  and  $4 \text{ mm}$ . This trace showed a sensitivity of  $0.156 \Omega/\text{mm}$  ( $GF = 0.007$ ) with a resolution of  $0.21 \text{ mm}$  (4.2% strain). A small amount of hysteresis was observed. The baseline DC resistance was  $118.7 \Omega$ . Mean and standard deviation were calculated using resistance measurements at  $0.05 \text{ mm}$  intervals.

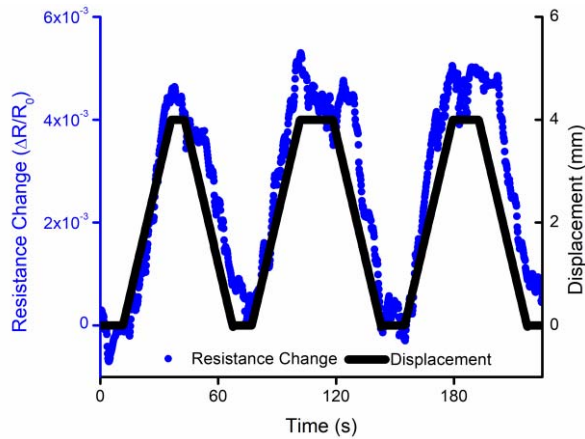


Fig. 7. The response of a strain sensor on a B-type kirigami device over its first three strain cycles. Despite high noise, there was no noticeable difference between the first strain cycle and subsequent strain measurements.

devices exceeded that of the simulation results, with B-type devices failing at 350% strain experimentally versus 236% in simulation and A-type devices failing at 101% strain experimentally versus 34% in simulation. Improved performance over model results may be due to fabrication variability, namely low lithography resolution and overetching, both of which would increase slit dimensions and result in higher elongation to break. The model also possessed inherent limitations, including the assumption that the Parylene substrate was isotropic instead of layered and the use of material properties from literature without adjusting for changes that might occur during fabrication. A more accurate mechanical model could be constructed using two Parylene C layers with gold traces, and thin-film Parylene C could be measured after undergoing lithography, reactive ion etching, and metal deposition to determine if thermal cycling during these processes significantly affected material properties.

The electrical integrity of traces failed much earlier, at a point which appeared to coincide with the transition between

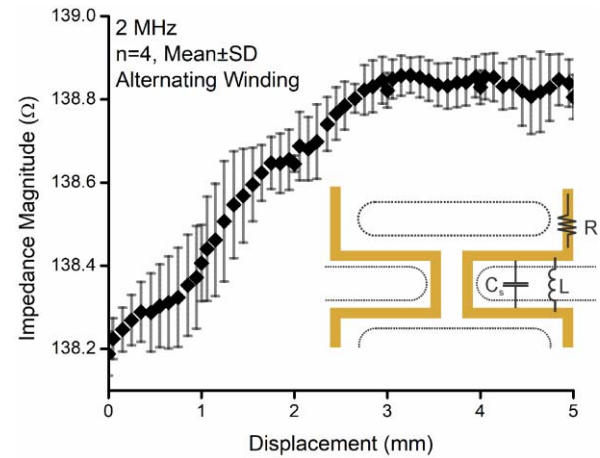


Fig. 8. High-frequency impedance magnitude versus displacement for a single trace on a B-type kirigami device. The impedance magnitude shows a non-linear relationship with displacement. Mean and standard deviation are calculated using impedance magnitudes measured at  $0.1 \text{ mm}$  intervals during strain cycling.

regions II and III as seen in force/displacement curves. Microcracks in Parylene were visible near the ends of each slit after stretching, and represent the likely cause of electrical failure. Electrical and mechanical tests confirm that increasing slit density enables high strain operation, but increasing inter-trace width does not improve the electrical stability of traces.

The DC resistance of traces on B-type devices varied quasilinearly with strain. This strain sensitivity likely resulted from stress within the thin-film gold traces, which concentrated at inflection points near the end of slits. DC resistance began to increase linearly as soon as strain was applied, but on some devices, the strain-resistance slope decreased after a sharp transition point, occurring around 60% strain. This drop could reduce overall sensitivity if a linear model is used and could cause measurement errors at the high end of the sensor's operating range. However, the largest contributor to sensor error is noise during individual measurements, and inaccuracy due to

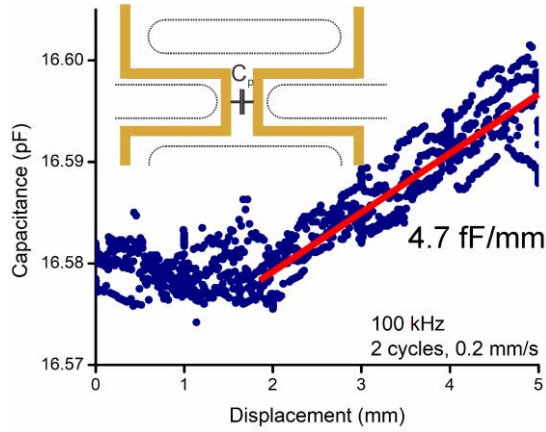


Fig. 9. The capacitance between two adjacent traces on a B-type kirigami device during two strain cycles to 5 mm, measured at 100 kHz. At around 2 mm displacement, capacitance begins to increase linearly with strain.

TABLE I

THIS WORK COMPARED TO OTHER PROPOSED FLEXIBLE STRAIN SENSORS [25], [26], [38]. BREAK STRAIN REFERS TO THE STRAIN AT WHICH MATERIALS FAILURE WAS REPORTED, WHILE ACTIVE STRAIN REFERS TO THE RANGE OVER WHICH STRAIN TRANSDUCTION WAS SUCCESSFULLY TESTED. CNTs = CARBON NANOTUBES, EGaln = EUTECTIC GALLIUM-INDIUM (LIQUID METAL)

	Break Strain	Active Strain	Gauge Factor	Thickness	Active Material
Park 2012	250%	100%	3.6	3500 $\mu\text{m}$	EGaln
Lee 2013	-	25%	22-100	1000 $\mu\text{m}$	CNTs
Firouzeh 2015	20%	12.5%	0.004	60 $\mu\text{m}$	Constantin
<b>This work</b>	<b>350%</b>	<b>80%</b>	<b>0.007</b>	<b>20 <math>\mu\text{m}</math></b>	<b>Gold</b>

the bilinear response in some traces will not significantly affect measurement accuracy until noise is reduced. Strategies for improving reproducibility between traces include using thicker metal layers and wider traces for increased trace stability and improving the placement of traces around kirigami slits using guidance from more advanced COMSOL simulations that directly model electrical traces during device stretching. Strategies for noise reduction include the use of more thermally stable conductive materials, improvements to the testing setup to further reduce vibration and provide a stable temperature during testing, and the implementation of signal filtering to eliminate high-frequency resistance variations.

Even without optimization, the sensitivity of resistance-based strain transduction is competitive with previously reported polyimide devices. Parylene devices possessed a higher dynamic range despite a conservative testing protocol (0.16  $\Omega/\text{mm}$  over 80% strain vs  $-0.18 \Omega/\text{mm}$  over 20% strain for polyimide sensors [25]). Construction from Parylene C and gold renders sensors not only resistant to corrosion but biocompatible and suitable for use in the human body. This contrasts with other reported strain sensors that utilize semiconductor-based piezoresistive materials [36], carbon nanotubes [26], [37], or liquid metal [38].

The scope of this study was limited to investigating the strain sensitivity of electrical traces embedded in thin-film

kirigami devices. Further work is needed to develop the kirigami devices presented in this work into practical strain sensors for biomedical applications. For example, it is important to investigate high-frequency operation of strain sensors for application involving rapid movement. Unfortunately, the testing setup available for strain transduction and evaluation was limited to a displacement rate of 0.2 mm/s. Future tests require the construction of a new testing setup for rapid strain cycling, and future studies will investigate the mechanical frequency response and bandwidth of optimized kirigami devices. Measurement noise was higher than desirable for precise strain measurements. High noise levels may have been due to thermal noise in the conductive trace or environmental noise in the testing setup. A small amount of hysteresis was observed, possibly due to polymer reorganization during device displacement. There was also a large difference in sensitivity between traces, even within the same device; the trace's position on the device did not appear to be the cause of these sensitivity differences. Further work is needed to determine the causes of sensitivity differences and to optimize trace designs for DC strain sensing.

Preliminary experiments indicate that both self-impedance and inter-trace capacitance increased with strain. Strain transduction via complex impedance or capacitance would be advantageous in the development of passive, wireless strain sensors. Increases in trace impedance were likely a result of variations in self-inductance within a trace. Changes in inter-trace capacitance may have resulted from varying either the separation between traces or the dielectric properties of Parylene C under stress. Future work will continue to explore high-frequency strain sensing with optimized devices, and will pair kirigami strain sensors with thin-film inductive coils [39] to develop passive, wireless strain sensors.

## VII. CONCLUSION

Using kirigami slit designs, devices were fabricated out of Parylene C and gold which could stretch to multiple times their length while maintaining electrical integrity of traces. The devices were found to have multiple electrical parameters which vary predictably with strain. DC resistance's sensitivity to strain was found to be of comparable sensitivity to previously reported polymer sensors but with a higher dynamic range and simpler trace geometry. Inter-trace capacitance and high-frequency inductance also varied with strain, which could lead to additional sensing modalities based off frequency transduction as opposed to resistive transduction. Construction out of only Parylene and gold renders these sensors not only resistant to corrosion but fully biocompatible and suitable for chronic implantation in the human body. This contrasts with other common strain sensors which utilize semiconductor-based piezoresistive materials or carbon nanotubes for strain sensing, neither of which is amenable to chronic implantation. A high dynamic range, low stress strain sensor could potentially be used in numerous biomedical applications.

## ACKNOWLEDGMENT

The authors would like to thank Jessica Ortigoza-Diaz for her help with testing and characterization, Dr. Donghai Zhu of



the Keck Photonics Laboratory for his assistance with fabrication, and all the members of the Biomedical Microsystems Lab of USC for their help and support.

## REFERENCES

- [1] T. Castle *et al.*, "Making the cut: Lattice kirigami rules," *Phys. Rev. Lett.*, vol. 113, no. 24, p. 245502, 2014.
- [2] S. J. P. Callens and A. A. Zadpoor, "From flat sheets to curved geometries: Origami and kirigami approaches," *Mater. Today*, vol. 21, no. 3, pp. 241–264, Apr. 2018.
- [3] R. M. Neville, F. Scarpa, and A. Pirrera, "Shape morphing kirigami mechanical metamaterials," *Sci. Rep.*, vol. 6, Aug. 2016, Art. no. 31067.
- [4] Y. Liu, K. He, G. Chen, W. R. Leow, and X. Chen, "Nature-inspired structural materials for flexible electronic devices," *Chem. Rev.*, vol. 117, no. 20, pp. 12893–12941, 2017.
- [5] M. Weston, "Anisotropic operations," *Int. J. Architect. Comput.*, vol. 10, no. 1, pp. 105–119, 2012.
- [6] Y. Zhang *et al.*, "Printing, folding and assembly methods for forming 3D mesostructures in advanced materials," *Nature Rev. Mater.*, vol. 2, no. 4, p. 17019, 2017.
- [7] Z. Song, *Studies of Origami and Kirigami and Their Applications*. Tempe, AZ, USA: Arizona State Univ., 2016.
- [8] Y. Zhang *et al.*, "A mechanically driven form of Kirigami as a route to 3D mesostructures in micro/nanomembranes," *Proc. Nat. Acad. Sci. USA*, vol. 112, no. 38, pp. 11757–11764, 2015.
- [9] Z. Song *et al.*, "Kirigami-based stretchable lithium-ion batteries," *Sci. Rep.*, vol. 5, Jun. 2015, Art. no. 10988.
- [10] K. K. Fu, J. Cheng, T. Li, and L. Hu, "Flexible batteries: From mechanics to devices," *ACS Energy Lett.*, vol. 1, no. 5, pp. 1065–1079, 2016.
- [11] A. Lamoureux, K. Lee, M. Shlian, S. R. Forrest, and M. Shtein, "Dynamic kirigami structures for integrated solar tracking," *Nature Commun.*, vol. 6, Sep. 2015, Art. no. 8092.
- [12] M. Ouisse, M. Collet, and F. Scarpa, "A piezo-shunted kirigami auxetic lattice for adaptive elastic wave filtering," *Smart Mater. Struct.*, vol. 25, no. 11, p. 115016, 2016.
- [13] L. Xu, X. Wang, Y. Kim, T. C. Shyu, J. Lyu, and N. A. Kotov, "Kirigami nanocomposites as wide-angle diffraction gratings," *ACS Nano*, vol. 10, no. 6, pp. 6156–6162, 2016.
- [14] Y. H. Chan, Z. Tse, and H. Ren, "Design evolution and pilot study for a kirigami-inspired flexible and soft anthropomorphic robotic hand," in *Proc. 18th Int. Conf. Adv. Robot. (ICAR)*, Jul. 2017, pp. 432–437.
- [15] J. Rossiter and S. Sareh, "Kirigami design and fabrication for biomimetic robotics," *Proc. SPIE*, vol. 9055, p. 90550G, Mar. 2014.
- [16] K. Zhang, C. Qiu, and J. S. Dai, "Helical kirigami-inspired centimeter-scale worm robot with shape-memory-alloy actuators," in *Proc. ASME Int. Design Eng. Tech. Conf. Comput. Inf. Eng. Conf.*, 2014, p. V05BT08A039.
- [17] C. Wu, X. Wang, L. Lin, H. Guo, and Z. L. Wang, "Based triboelectric nanogenerators made of stretchable interlocking kirigami patterns," *ACS Nano*, vol. 10, no. 4, pp. 4652–4659, 2016.
- [18] S. Sareh and J. Rossiter, "Kirigami artificial muscles with complex biologically inspired morphologies," *Smart Mater. Struct.*, vol. 22, no. 1, p. 014004, 2012.
- [19] M. Isobe and K. Okumura, "Initial rigid response and softening transition of highly stretchable kirigami sheet materials," *Sci. Rep.*, vol. 6, Apr. 2016, Art. no. 24758.
- [20] M. K. Blees *et al.*, "Graphene kirigami," *Nature*, vol. 524, no. 7564, p. 204, 2015.
- [21] T. C. Shyu *et al.*, "A kirigami approach to engineering elasticity in nanocomposites through patterned defects," *Nature Mater.*, vol. 14, no. 8, p. 785, 2015.
- [22] Z. Qi, D. K. Campbell, and H. S. Park, "Atomistic simulations of tension-induced large deformation and stretchability in graphene kirigami," *Phys. Rev. B, Condens. Matter*, vol. 90, no. 24, p. 245437, 2014.
- [23] Y. Morikawa *et al.*, "Ultrastretchable kirigami bioprobes," *Adv. Healthcare Mater.*, vol. 7, no. 3, p. 1701100, 2018.
- [24] Y. Morikawa, S. Yamagiwa, H. Sawahata, M. Ishida, and T. Kawano, "An origami-inspired ultrastretchable bioprobe film device," in *Proc. IEEE 29th Int. Conf. Micro Electro Mech. Syst. (MEMS)*, Jan. 2016, pp. 149–152.
- [25] A. Firouzeh and J. Paik, "The design and modeling of a novel resistive stretch sensor with tunable sensitivity," *IEEE Sensors J.*, vol. 15, no. 11, pp. 6390–6398, Nov. 2015.
- [26] C. Lee, L. Jug, and E. Meng, "High strain biocompatible polydimethylsiloxane-based conductive graphene and multiwalled carbon nanotube nanocomposite strain sensors," *Appl. Phys. Lett.*, vol. 102, no. 18, p. 183511, Apr. 2013.
- [27] C. Hassler, R. P. von Metzzen, P. Ruther, and T. Stieglitz, "Characterization of parylene C as an encapsulation material for implanted neural prostheses," *J. Biomed. Mater. Res. B, Appl. Biomater.*, vol. 93, no. 1, pp. 266–274, 2010.
- [28] R. P. von Metzzen and T. Stieglitz, "The effects of annealing on mechanical, chemical, and physical properties and structural stability of Parylene C," *Biomed. Microdevices*, vol. 15, no. 5, pp. 727–735, 2013.
- [29] B. J. Kim and E. Meng, "Review of polymer MEMS micromachining," *J. Micromech. Microeng.*, vol. 26, no. 1, p. 013001, 2016.
- [30] B. J. Kim and E. Meng, "Micromachining of Parylene C for bioMEMS," *Polym. Adv. Technol.*, vol. 27, no. 5, pp. 564–576, May 2016.
- [31] *Specialty Coating Systems*, SP Properties, Indianapolis, IN, USA, 2011.
- [32] E. Meng, P.-Y. Li, and Y.-C. Tai, "Plasma removal of Parylene C," *J. Micromech. Microeng.*, vol. 18, no. 4, p. 045004, 2008.
- [33] C. A. Gutierrez, C. Lee, B. Kim, and E. Meng, "Epoxy-less packaging methods for electrical contact to parylene-based flat flexible cables," in *Proc. 16th Int. Solid-State Sens., Actuators Microsyst. Conf. (TRANSDUCERS)*, Jun. 2011, pp. 2299–2302.
- [34] Y. Ma, X. Feng, J. A. Rogers, Y. Huang, and Y. Zhang, "Design and application of 'J-shaped' stress-strain behavior in stretchable electronics: A review," *Lab Chip*, vol. 17, no. 10, pp. 1689–1704, 2017.
- [35] S. C. Redshaw, "The electrical measurement of strain," *Aeronaut. J.*, vol. 50, no. 428, pp. 568–612, 1946.
- [36] J. Sirohi and I. Chopra, "Fundamental understanding of piezoelectric strain sensors," *J. Intell. Mater. Syst. Struct.*, vol. 11, no. 4, pp. 246–257, Apr. 2000.
- [37] T. Yamada *et al.*, "A stretchable carbon nanotube strain sensor for human-motion detection," *Nature Nanotechnol.*, vol. 6, no. 5, p. 296, 2011.
- [38] Y.-L. Park, B.-R. Chen, and R. J. Wood, "Design and fabrication of soft artificial skin using embedded microchannels and liquid conductors," *IEEE Sensors J.*, vol. 12, no. 8, pp. 2711–2718, Aug. 2012.
- [39] A. Baldwin, L. Yu, M. Pratt, K. Scholten, and E. Meng, "Passive, wireless transduction of electrochemical impedance across thin-film microfabricated coils using reflected impedance," *Biomed. Microdevices*, vol. 19, no. 4, p. 87, 2017.



Alex Baldwin received the B.S. degree in electrical engineering from the University of Arkansas, Fayetteville, in 2013, and the M.S. and Ph.D. degrees in biomedical engineering from the University of Southern California (USC) in 2015 and 2018, respectively. He is currently involved in improving the treatment of hydrocephalus using chronically implanted wireless sensors. His research interests include polymer micromachining, implantable biomedical sensors, and novel microelectromechanical devices, which operate using electrochemical impedance. He was a recipient of the USC Viterbi Fellowship and the Alfred E. Mann Institute Fellowship.



Ellis Meng (M'02–SM'09–F'16) received the B.S. degree in engineering and applied science and the M.S. and Ph.D. degrees in electrical engineering from the California Institute of Technology (Caltech), Pasadena, in 1997, 1998, and 2003, respectively. She also holds a joint appointment with the Ming Hsieh Department of Electrical Engineering. She has been a Professor of biomedical engineering with the University of Southern California, Los Angeles, since 2004. Her research interests include bioMEMS, implantable biomedical microdevices, microfluidics, multimodality integrated microsystems, and packaging. She is a fellow of ASME, BMES, and AIMBE. She is a member of the Tau Beta Pi, the Biomedical Engineering Society, the Society of Women Engineers, and the American Society for Engineering Education. She was a recipient of the Intel Women in Science and Engineering Scholarship, the Caltech Alumni Association Donald S. Clark Award, and the Caltech Special Institute Fellowship. She has also received the NSF CAREER Award and the Wallace H. Coulter Foundation Early Career Translational Research Award. In 2009, she was recognized as one of the TR35 Technology Review Young Innovators under 35. She was the Viterbi Early Career Chair of the Viterbi School of Engineering and the Department Chair from 2015 to 2018.